Detection of microseismic compressional (P) body waves aided by numerical modeling of oceanic noise sources

Mathias Obrebski, Fabrice Ardhuin, Eleonore Stutzmann, Martin Schimmel

JOURNAL OF GEOPHYSICAL RESEARCH: SOLID EARTH, VOL. 118, 4312–4324, doi:10.1002/jgrb.50233, 2013

Detection of microseismic compressional (*P*) body waves aided by numerical modeling of oceanic noise sources

Mathias Obrebski,[1,2,3] Fabrice Ardhuin,[1] Eleonore Stutzmann,[4] and Martin Schimmel[5]

Received 30 January 2013; revised 29 May 2013; accepted 30 May 2013; published 27 August 2013.

[1] Among the different types of waves embedded in seismic noise, body waves present appealing properties but are still challenging to extract. Here we first validate recent improvements in numerical modeling of microseismic compressional (*P*) body waves and then show how this tool allows fast detection and location of their sources. We compute sources at ~0.2 Hz within typical *P* teleseismic distances (30–90°) from the Southern California Seismic Network and analyze the most significant discrete sources. The locations and relative strengths of the computed sources are validated by the good agreement with beam-forming analysis. These 54 noise sources exhibit a highly heterogeneous distribution, and cluster along the usual storm tracks in the Pacific and Atlantic oceans. They are mostly induced in the open ocean, at or near water depths of 2800 and 5600 km, most likely within storms or where ocean waves propagating as swell meet another swell or wind sea. We then emphasize two particularly strong storms to describe how they generate noise sources in their wake. We also use these two specific noise bursts to illustrate the differences between microseismic body and surface waves in terms of source distribution and resulting recordable ground motion. The different patterns between body and surface waves result from distinctive amplification of ocean wave-induced pressure perturbation and different seismic attenuation. Our study demonstrates the potential of numerical modeling to provide fast and accurate constraints on where and when to expect microseismic body waves, with implications for seismic imaging and climate studies.

Citation: Obrebski, M., F. Ardhuin, E. Stutzmann, and M. Schimmel (2013), Detection of microseismic compressional (*P*) body waves aided by numerical modeling of oceanic noise sources, *J. Geophys. Res. Solid Earth*, *118*, 4312–4324, doi:10.1002/jgrb.50233.

1. Introduction

[2] Microseisms, referring to the background noise recorded by seismic stations during periods of earthquakes quiescence, have become an important source of information for seismic imaging and climate analysis. At frequencies between 0.05 and 0.3 Hz, microseisms are induced by sea states. In particular, ocean wave-wave interactions excite seismic waves at twice the frequency of ocean waves ("secondary microseisms" or "double-frequency microseisms," DFM hereafter). As described in theoretical studies, DFM produce a strong signal between 0.1 and 0.3 Hz both as surface waves [*Miche*, 1944; *Longuet-Higgins*, 1950; *Hasselmann*, 1963] and as body waves [*Ardhuin and Herbers*, 2013]. Compared to ballistic seismic waves (i.e., exited by earthquakes), the sources of the microseismic wave field are more widely distributed in space and time. These advantages explain the recent keen interest in exploiting seismic noise to illuminate the elastic structure of the earth [*Shapiro and Campillo*, 2004; *Shapiro et al*., 2005; *Sabra et al.*, 2005] and its transient variations attributable to volcanic and seismic activity [*Brenguier et al*., 2008a, 2008b; *Durand et al*., 2011; *Rivet et al*., 2011]. Taking advantage of the link between sea states and microseisms, noise records are also analyzed to detect seasonal or long-term variations, interpreted in turn as changes in climate [*Bromirski et al*., 1999; *Grevemeyer et al*., 2000; *Aster et al*., 2008, 2010; *Stutzmann et al*. 2009, 2012; *Ebeling and Stein*, 2011; *Ardhuin et al*., 2012; *Traer et al*., 2012]. For this specific purpose, the main advantage of seismic records over satellite and buoys measurements stems from the early and wide deployment of seismic stations all over the globe since 1960.

[3] Body waves have appealing properties compared to the surface waves that dominate the DFM spectra. Body and surface waves travel through the Earth and along its surface, respectively. Consequently, seismic tools like beam-forming analysis (BFA hereafter) allow one to locate the source of body waves, while only the back azimuth (direction to the source) is generally resolved for surface waves [*Haubrich and McCamy*,

[1]Laboratoire d'Océanographie Spatiale, Ifremer, Plouzané, France.
[2]LHEEA, Ecole Centrale de Nantes, LUNAM University, Nantes, France.
[3]Now at Lamont-Doherty Earth Observatory, Columbia University, Palisades, New York, USA.
[4]IPGP, PRES Université Paris-Cité, Paris, France.
[5]Institute of Earth Sciences Jaume Almera, CSIC, Barcelona, Spain.

Corresponding author: M. Obrebski, Lamont-Doherty Earth Observatory, Columbia University, Palisades, NY 10964, USA. (obrebski@ldeo.columbia.edu)

2169-9313/13/10.1002/jgrb.50233

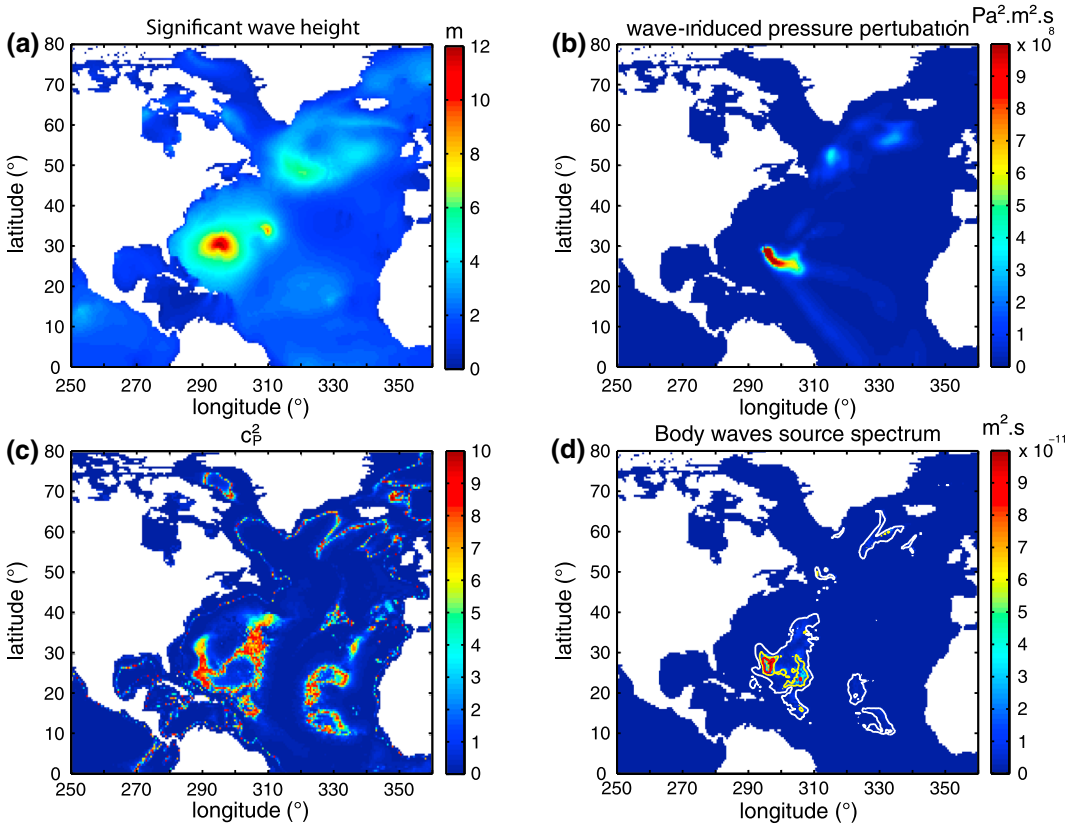

Figure 1. Numerical modeling of wave-induced double-frequency compressional (*P*) waves on 19 September 2010, 12:00:00 and at the seismic frequency 0.193 Hz. (a) Map of the ocean significant wave height that shows a storm along the east coast of the U.S. (b) Ocean wave-wave interactions induce second-order pressure perturbation (F_{p3D} in equation (2)). (c) These long wavelength oscillations are coupled with the ocean crust with an efficiency described by a coupling coefficients c_P^2. (d) The resulting *P* wave sources ($F_{\delta,P}$ in equation (3)).

1969; *Chevrot et al*., 2007; *Koper and de Foy*, 2008; *Gerstoft and Tanimoto*, 2007; *Gerstoft et al*., 2008; *Koper et al*., 2009, 2010]. This has important implications, for example, when using noise as an indicator of sea states [*Zhang et al*., 2010b]. As for the specific purpose of seismic imaging, the inversion of surface wave properties typically leads to a smoothed image of the Earth structure. In contrast, the analysis of reflected and refracted body waves provides tighter constraints on sharp velocity discontinuities.

[4] The analysis and use of microseismic body waves is still challenging. This results from surface waves largely dominating the recorded noise spectrum [*Haubrich et al*., 1963]. The detection of microseismic body waves is typically performed through BFA, which is a powerful data-driven tool that allows quantifying and discriminating the incoming amount of energy as a function of back azimuth and wave slowness (and thus wave type). Nonetheless, BFA can be time consuming if data mining is performed randomly. In addition, BFA requires a 2-D dense seismic array, which constitutes an important limitation. If seismic imaging is the ultimate goal, specific processing of long noise records allows resolving body waves travel times between pairs of stations [*Roux et al*., 2005; *Schimmel et al*., 2011a; *Poli et al*., 2012]. As shown by *Zhang et al*. [2010a], travel times can also be resolved using considerably shorter noise records, but this requires detecting and locating loud noise bursts, which in turns implies performing BFA with the limitations described above.

[5] Our objectives are first to validate recent advances in numerical modeling of microseismic sources of compressional (*P*) body waves (just "*P* waves" hereafter) and then to illustrate the potential of our numerical approach to guide the search for source occurrence and thus to avoid random data mining with BFA. Numerical models for microseismic surface waves have been developed from numerical models of ocean waves [*Kedar et al*., 2008; *Ardhuin et al*., 2011]. Here we extend previous works to simulate the noise generation specific to *P* waves using the theory given by *Ardhuin and Herbers* [2013]. In the first section, we briefly review how the ocean wave numerical model is modified to simulate ocean wave-wave interactions and the resulting "double-frequency microseisms." We also present the BFA method used to validate the computed locations based on real seismic data. We then use the noise numerical model to detect and provide the first location catalogue of the significant *P* wave sources generated around the Southern California Seismic Network (SCSN) during 2010. We describe in more details two particularly strong events that took place in the Pacific and Atlantic oceans. We finally discuss how the distribution of *P* wave sources relates with storms. We also compare the

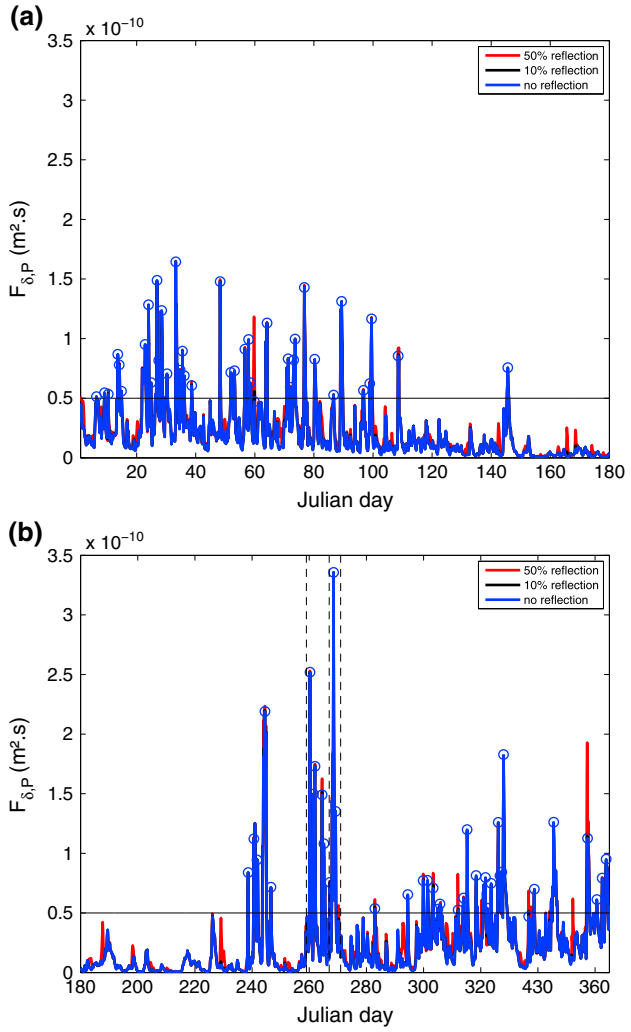

Figure 2. (a and b) Maximum of the computed sources of microseismic *P* waves as a function of time. The values are extracted from the numerical model ($F_{\delta,P}$ in equation (3)) at seismic frequency 0.193 Hz. We only compute sources within 30° and 90° from the Southern California Seismic Network. All noise events producing a source peak above the horizontal dashed line are analyzed. The vertical dashed lines in Figure 2b bound two particularly strong events that occurred between 16 September 2010 (Julian day 259) and 27 September 2010 (Julian day 270) and are depicted in Figures 4 and 5.

distribution of *P* sources with that of surface waves simultaneously generated and recorded during the two strong events mentioned above.

2. Method and Data

[6] Here we describe the noise numerical model (section 2.1) and the beam-forming analysis used to validate the *P* wave source locations (section 2.2). An analysis of the whole double-frequency microseismic frequency band (0.1–0.3 Hz) is beyond the scope of the current study. To choose a single frequency to conduct our analysis, we performed a preliminary beam-forming analysis of several significant noise events at frequencies between 0.1 and 0.3 Hz and observed that the strongest *P* wave signature was around 0.2 Hz at the Southern California Seismic Network. We will explain this feature from the theory of body wave excitation in section 4.3. Therefore, we chose the frequency 0.193 Hz (the closest discrete value of our numerical model) to perform all the modeling and analysis described in the following sections, without loss of generality.

2.1. Seismic Noise Modeling

[7] To assess the distribution of DFM, we use a numerical approach based on the WAVEWATCH III® framework [*Tolman*, 2008; *Ardhuin et al.*, 2010]. The second-order pressure spectrum generated by nonlinear interaction between ocean waves with similar frequency and traveling in opposite direction (Figure 1b) is computed from the wave frequency spectrum $E(f)$ and the directional integral $I(f)$ that depends only on the ocean wave energy distribution M over the direction θ [*Ardhuin et al.*, 2011],

$$I(f) = \int_0^{\pi} M(f,\theta) \times M(f,\pi+\theta)\mathrm{d}\theta \tag{1}$$

[8] Following *Hasselmann* (1963), the pressure power spectrum at seismic frequency $f_s = 2f$, where f is the ocean wave frequency, and $k_s = k - k'$, the difference between the wave number of ocean waves propagating in almost opposite directions, is given in deep water by

$$F_{p3D}(k_s \cong 0, f_s = 2f) = \rho_w^2 g^2 f_s E^2(f) I(f) \tag{2}$$

where ρ_w is the water density. An important aspect of our model is that the possibly significant effect of coastal ocean wave reflection is taken into account in the calculation of $E(f)$ and $I(f)$. In general, this reflection can be represented by a wave amplitude reflection coefficient, that is, a function of the wave height, wave frequency, and the bottom slope on the shore [*Ardhuin and Roland*, 2012]. In order to limit errors associated with the poor knowledge of bottom slopes for the entire globe, we adjust the coastal reflection by combining a model with and without a constant reflection as done in the study by *Ardhuin et al.* [2011]. This approach to coastal reflection is simplistic, as the bottom slope varies from cliffs to beaches. Work is in progress to improve the global database of slopes, allowing the use of a more realistic parameterization for coastal reflection.

[9] At this point, the theory branches out for the different seismic wave types. Contrary to *Hillers et al.* [2012] who used maps of Rayleigh-wave sources and assumed they conformed to *P* wave sources, here we consider the theory for *P* waves, with a power spectrum of the vertical displacement at the top of the crust given by *Ardhuin and Herbers* [2013] from the local ocean waves.

$$F_{\delta,P}(f_s) \cong \frac{F_{p3D}(f_s)}{\rho_s^2 \beta^4} c_P^2 \tag{3}$$

where ρ_s is the crustal density, β the shear wave speed, and c_p a nondimensional coefficient that amplifies the wave-induced pressure into ground displacement associated with *P* waves

Table 1. List of Most Significant Events That Occurred During 2010 Within 30–90° From the Southern California Seismic Network[a]

Year	Julian day	Month	Day	Hour	SL (m^4.s)	LAT_{TH} (°)	LON_{TH} (°)	LAT_{BFA} (°)	LON_{BFA} (°)	$D_{TH/BFA}$ (°)	Rank
2010	6	1	6	9	7.0	41.0	152.5	40.8	151.7	4.0	1
2010	13	1	13	15	3.4	44.5	153.0	43.7	156.7	9.3	1
2010	22	1	22	21	8.7	37.7	−170.0	38.2	−167.4	3.3	1
2010	24	1	24	21	3.5	35.0	169.5	36.8	170.6	9.5	1
2010	28	1	28	12	3.9	46.5	175.0	46.8	174.3	3.8	1
2010	30	1	30	6	6.5	48.5	161.0	47.9	164.5	5.1	1
2010	33	2	2	6	5.4	39.5	155.5	39.5	154.7	7.4	1
2010	34	2	3	18	6.3	42.0	157.5	41.7	158.1	1.5	1
2010	35	2	4	12	2.4	39.0	−55.5	38.9	−56.1	1.2	2
2010	36	2	5	3	0.5	43.0	−49.0	43.1	−47.5	7.0	2
2010	38	2	7	15	4.1	39.5	167.0	40.1	164.3	3.3	1
2010	51	2	20	21	5.8	47.0	168.5	47.0	−179.5	3.7	1
2010	53	2	22	3	3.3	44.0	168.5	45.4	173.4	5.0	1
2010	56	2	25	15	3.9	29.0	169.5	28.8	168.5	3.6	1
2010	59	2	28	21	0.8	59.0	171.5	51.2	173.2	9.5	1
2010	64	3	5	3	2.7	52.0	−171.5	49.0	−176.8	5.7	1
2010	71	3	12	6	3.4	48.5	171.0	47.1	164.5	3.9	1
2010	73	3	14	3	0.6	−12.5	−179.5	−12.3	−179.4	2.5	2
2010	73	3	14	15	0.6	−14.0	−180.0	−13.4	−179.7	2.4	1
2010	76	3	17	18	4.1	−31.0	−169.5	−30.6	−170.3	5.2	1
2010	80	3	21	6	5.7	47.0	−175.5	47.1	−175.4	3.3	1
2010	86	3	27	15	3.5	48.5	159.0	48.6	161.4	2.4	1
2010	89	3	30	9	5.6	40.5	165.0	39.9	162.1	6.7	1
2010	98	4	8	21	2.3	49.0	166.0	46.4	164.1	5.3	1
2010	108	4	18	12	3.5	43.0	159.5	42.6	158	3.7	1
2010	145	5	25	15	7.4	−42.5	−140.5	−42.0	−141.9	1.5	1
2010	238	8	26	15	0.5	23.5	−55.5	23.3	−55.2	3.6	1
2010	240	8	28	15	0.7	29.0	−61.0	28.9	−61.1	5.9	1
2010	241	8	29	18	2.5	36.5	−56.0	35.1	−56.1	4.2	1
2010	244	9	1	12	4.3	24.0	−71.0	23.7	−70.5	2.1	1
2010	260	9	17	6	2.2	22.0	−58.5	21.9	−58.4	1.6	1
2010	261	9	18	12	0.9	25.5	−63.5	25.4	−63.4	4.3	1
2010	262	9	19	0	2.3	27.0	−64.0	26.5	−64	5.1	1
2010	264	9	21	12	0.6	44.0	−58.0	42.6	−57	5.3	1
2010	267	9	24	6	0.5	25.5	141.0	25.3	141.1	4.5	2
2010	268	9	25	12	7.3	39.0	147.5	38.0	146.6	4.8	1
2010	269	9	26	6	1.6	44.5	153.0	42.3	151.5	8.6	1
2010	312	11	8	3	1.9	62.0	−20.0	62.3	−21.7	3.2	2
2010	314	11	10	0	2.9	40.5	−161.0	40.0	−161.4	3.9	1
2010	318	11	14	9	2.1	41.0	170.5	41.3	169.5	1.1	1
2010	322	11	18	9	0.6	56.5	−13.5	58.5	−12.8	3.4	2
2010	326	11	22	3	0.5	61.5	−60.0	60.8	−59.6	4.4	2
2010	326	11	22	18	14.6	46.0	−169.0	43.1	−167.9	2.2	1
2010	327	11	23	9	13.9	51.5	−170.0	44.1	−165.8	4.0	1
2010	328	11	24	0	7.4	40.0	148.5	39.7	148.5	3.2	2
2010	338	12	4	18	3.1	38.0	−31.0	38.2	−30.9	2.6	2
2010	345	12	11	12	12.7	38.0	169.5	41.6	165.7	3.2	1
2010	360	12	26	15	2.9	60.0	−27.5	59.1	−30.5	3.8	2
2010	362	12	28	12	4.2	47.5	172.5	47.1	173	5.8	1
2010	363	12	29	21	10.6	42.0	155.0	41.4	154.6	1.5	1
2010	365	12	31	3	8.0	45.0	175.0	43.4	171.2	4.8	1

[a]All events are first detected using the noise numerical model (circled maxima in Figure 2). We then perform beam-forming analysis at the SCSN to validate their location. The first five columns give the timing of each noise event (maximum computed source). "SL" is the source level (see definition text). "LAT_{TH}," "LON_{TH}," "LAT_{BFA}," and "LON_{BFA}" define the location of the computed sources centroid and the geographical projection of the beam-former maximum, respectively. "$D_{TH/BFA}$" is the distance between these locations. The last column indicates whether the event appears in the beam-former output as the main peak (rank 1) or a secondary peak (rank 2).

(Figure 1c). In equation (3), the ground displacement has been summed over all take-off angles. The angle-dependent expression is given by *Ardhuin and Herbers* [2013]. For the sake of simplicity, hereafter we will refer to $F_{\delta,P}$ as the body wave "sources." The theory for surface wave generation [*Miche*, 1944; *Longuet-Higgins*, 1950; *Hasselmann*, 1963] as implemented by *Ardhuin et al*. [2011] is summarized in Appendix A. *Ardhuin and Herbers* [2013] showed that, in theory, the generation of microseismic body and surface waves are intrinsically different, with distinct amplifying coefficients (compare Figure 1c and Figure A1a). This difference is illustrated and discussed in section 4.3 with real noise events.

[10] We finally define the source level as the sum (integral over space) of all computed sources with $F_{\delta,P} \geq 0.1 \times F_{\delta,P}^{\max}$ (equation (3)). A quantitative estimation of the resulting ground motion at a given seismic station requires a propagation model or the direct estimation of solid Earth motions (e.g., *Gualtieri et al*. [2013]) and is beyond the scope of this study.

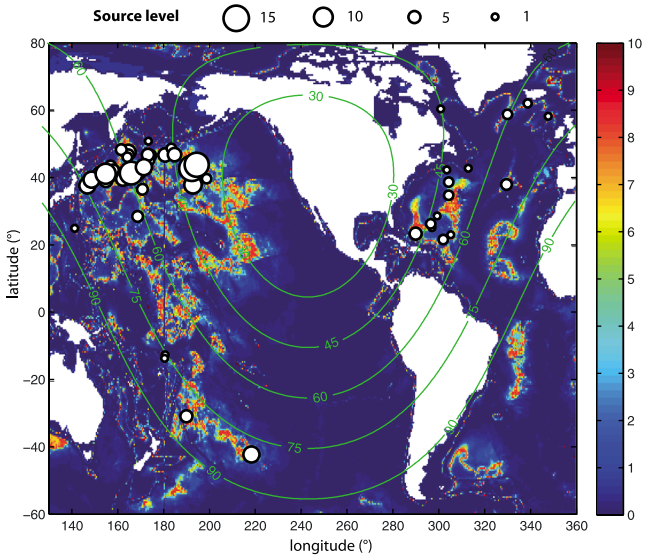

Figure 3. Map of microseismic *P* wave sources. The timing of microseismic events is given by the numerical model (Figure 2), but their location is estimated solely by using beam-forming analysis. The white dots mark the geographical projections of the beam-former output maxima. The dots size is scaled according to the corresponding source level (SL in Table 1). The background image maps the coupling coefficient c_P^2 for *P* waves. Green contours indicate the distance (in degrees) from the SCSN center.

2.2. Beam-Forming Analysis

[11] To validate the location of *P* wave sources as computed by the noise model, we use the standard (or Bartlett) beam-forming analysis (BFA) (see review by *Rost and Thomas* [2002]) at the Southern California Seismic Network (SCSN). The idea of this approach is to decompose the wave field at the seismic array into a slowness and direction spectrum, using the phase delays between all pairs of stations. This method is thus suitable to detect all types of seismic waves. For an incoming wave $y_i(\boldsymbol{s})$, $\boldsymbol{s}$ being the slowness vector, the phase vector is defined as

$$\Psi = \begin{bmatrix} \psi_1 \\ \vdots \\ \psi_{N_S} \end{bmatrix} \quad with \quad \psi_i(\boldsymbol{s}) = e^{i\omega_0 s r_i} \tag{4}$$

[12] Vector $\boldsymbol{r_i}$ represents the coordinate of station *i* in the array reference frame, and ω_0 is the angular frequency at which we perform the beam-forming analysis. We define $d(\omega_0)_i$ the component of the Fourier transform $Y(\omega)_i$ of the seismic record at station *i* at angular frequency ω_0. The data vector is

$$\boldsymbol{d} = \begin{bmatrix} d(\omega_0)_1 \\ \vdots \\ d(\omega_0)_{N_S} \end{bmatrix} \tag{5}$$

[13] The beam former $BF(\boldsymbol{s})$ represents the projection of the spectral energy at angular frequency ω_0 along the slowness vector $\boldsymbol{s}$:

$$BF(\boldsymbol{s}) = \Psi^T K \Psi \quad with \quad K = \boldsymbol{d}\boldsymbol{d}^T \tag{6}$$

The *P* waves are distinguished from other waves based on their slowness (0.04–0.1 s/km). Note that *PP* waves are observed in the same slowness range as *P* waves. Therefore, if *P* waves were detected based on BFA only, an ambiguity on the wave type would exist. Here we apply the opposite approach. We use the numeral model to detect *P* wave sources and then validate their location through BFA. Even though we cannot discard that *PP* waves are incidentally recorded when and where the model indicates *P* waves, the probability is low. *Gerstoft et al.* [2008] showed that microseismic core refracted waves (PKP) can be detected at slowness below 0.04 s/km. Although we do observe such waves (see Figure 5f, for example), we do not analyze them here.

[14] We use 24 h long time series around the computed source maxima. Seismic data were downloaded from the Southern California Earthquake Data Center. The waveforms are checked to detect earthquakes, instrument glitches, or failure. We truncate signals with amplitude larger than four times the daily standard deviation. The BFA is performed using 8 minute long slots. The number of seismic traces varies from 71 to 161, and is 146 on average. The resulting 24*60/8 = 180 beam-former outputs are then averaged to reduce the statistical uncertainty on the cospectra estimates, which results in sharper peaks. We use a slowness step of 0.0023 s/km and a frequency step of 0.002 Hz for the Fourier transformation of the seismic traces ($Y(\omega)_i$). Beam-former outputs are found to be consistent between adjacent frequencies. Therefore, we calculate the beam formers at three frequencies (0.191, 0.193, and 0.195 Hz) and average them, with a view to reducing the relative contributions of transient signals. The location of any peak of interest is then converted to a source location (BFA location hereafter) using the corresponding back-azimuth, horizontal slowness, and the velocity model ak135 [*Kennett et al.*, 1995]. The interstation distance varies from 10 to 625 km. The Bartlett BFA has a poor capability to separate sources from not too distant locations. For a typical compression speed of 5 km/s,

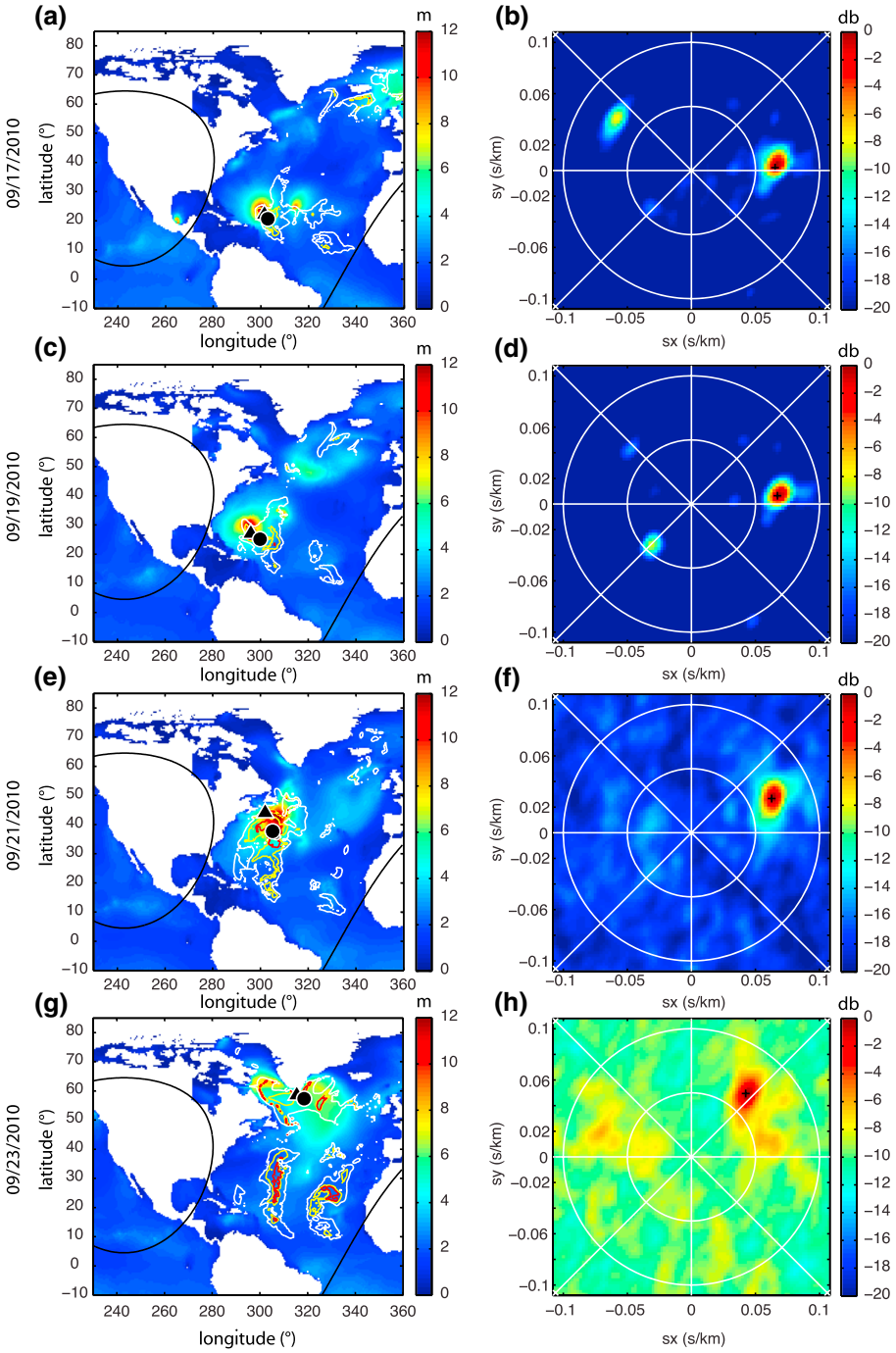

Figure 4. Sources of microseismic *P* wave during a particularly loud noise event in the North Atlantic from 16 to 23 September 2010. Each row corresponds to a specific day. (a,c,e,g) Map of the computed ocean wave height at noon (background image), contours of the daily average of microseismic sources (the white, yellow, and red lines contain 90%, 60%, and 30% of the strongest sources, respectively), the location of the maximum of these sources (black triangle), and the source location from beam-forming analysis (black dot) are combined. (b,d,f,h) Corresponding beam-former outputs (normalized by the maximum) obtained on a 24 h long basis.

the array spans 25 wavelengths for a frequency of 0.2 Hz. This gives a resolution of $\pi/50 = 0.06$ rad [*Krim and Viberg*, 1996], which translates into a typical resolution of 350 km in the azimuthal direction and a much larger distance of the order of 3700 km in the range direction [see, e.g., *Zhang et al.*, 2010a, Figure 1].

3. Results

[15] Here we describe the distribution of the most significant *P* wave sources detected using our numerical noise model, the location of which is validated by beam-forming analysis using real data. Figure 2 shows the value of the

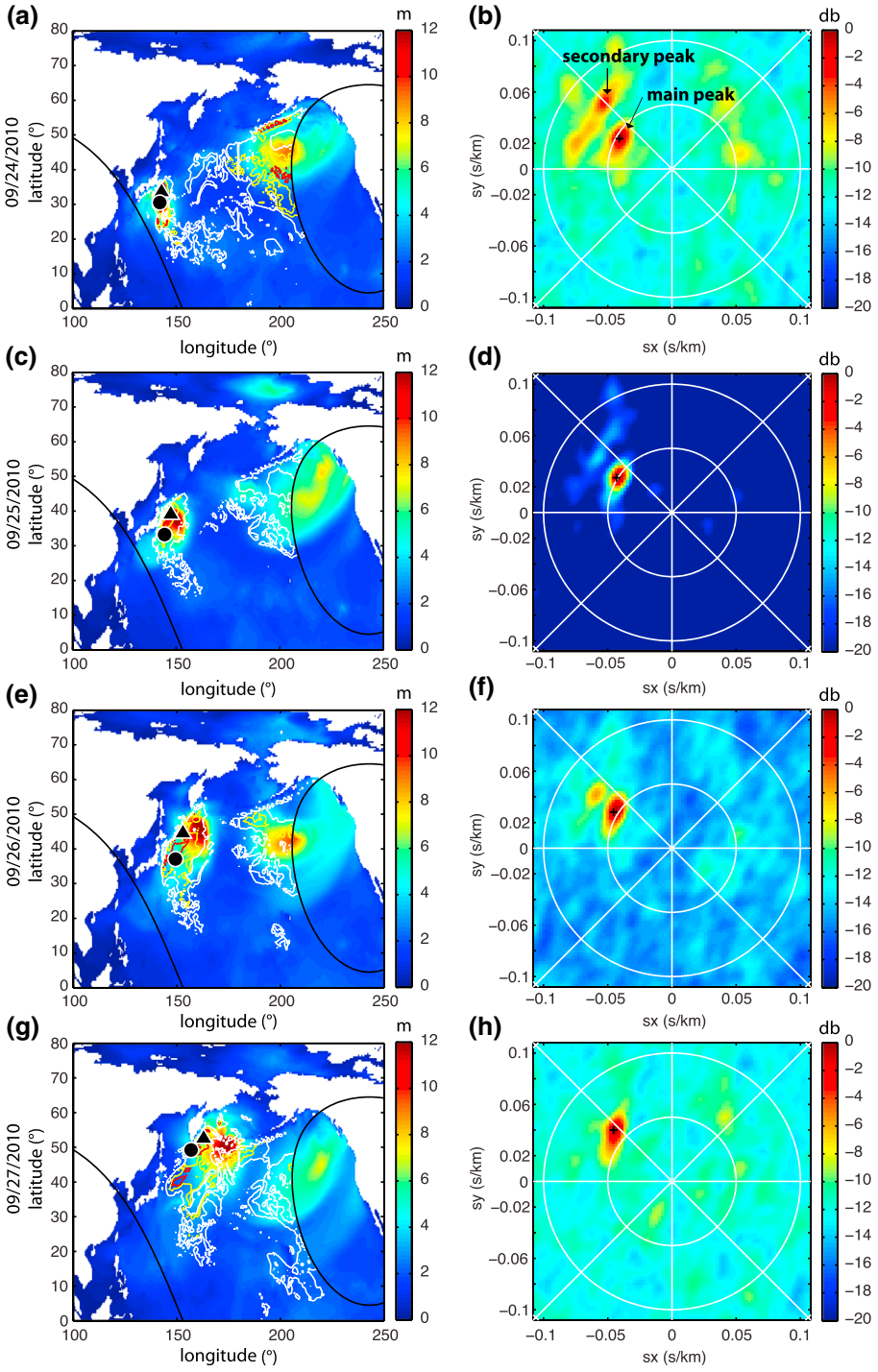

Figure 5. (a–h) Same as Figure 4 for the microseismic event that occurred in the Pacific Ocean between 24 and 27 September 2010.

maximum of the power spectrum of the vertical displacement at the top of the crust ($F_{\delta,P}$ in equation (3)) of *P* waves as a function of time during year 2010. We bound our modeling to all sources located between 30 and 90° from the center of the SCSN, which is the typical range to observe teleseismic *P* waves. We perform this computation using a conservatively high coastal reflection coefficient $R^2 = 10\%$. We focus on the most significant events by analyzing all peaks with amplitude larger than 0.5×10^{-10} $m^2.s$ (the horizontal line in Figure 2). From the original selection of 78 (computed) sources (circled maxima in Figure 2), in 54 cases, the beam-forming analysis yields a noticeable peak (at least 3 dB above the beam-former background) and its geographical projection is correlated with the location of the centroid of the computed sources. Quantifying the agreement between the source locations from the BFA and the

numerical model is complex. The width of the beam-former peak is controlled by the intrinsic resolution of the seismic array and the coherence and size of the noise source. As for the model, note that we detect the noise events using the maximum punctual source at each model time step, but the source region can be wide (see source contours in Figure 1d). We consider that the computed and BFA locations are correlated when the distance between them ($D_{TH/BFA}$ in Table 1) is smaller than 10°. For the 54 events in Table 1 and Figure 3, $1.1 < D_{TH/BFA} < 9.5°$ (mean value $4.2 \pm 2°$).

[16] Note that there is no direct link between the BFA amplitude at the array and the amplitude at the microseismic source because the incoming seismic energy effectively measured reflects not only the source level but also its size and is further affected by energy losses along the seismic path and imperfect coherence. Therefore, when multiple noise sources are simultaneously active, the strongest computed source may appear as a secondary peak in the beam-former output. We found several such situations (rank 2 in Table 1, see, for example, Julian day 35).

[17] Overall, at the specific frequency of 0.193 Hz, the *P* waves detected through BFA at the SCSN come mainly from the northern Pacific and to a lesser extent, from the northern Atlantic, which is in agreement from earlier BFA results of *Gerstoft et al*. [2008].

[18] The distribution of the strongest *P* wave sources is highly heterogeneous and clearly clusters along the usual storm tracks. To further illustrate this view, we describe in more details two particularly strong noise events that occurred from 16 to 23 September 2010 in the Atlantic Ocean (Figure 4) and from 24 to 27 September 2010 in the Pacific Ocean (Figure 5). We first note that there is a good agreement in time and space between the storm location (ocean wave height maxima) and the *P* wave source location. This consistency holds even in cases of multiple sources. During the Pacific event, a secondary peak appears in the beam-former outputs (Figures 5b–5f), and it points toward noise sources induced by a storm in the Gulf of Alaska. The noise model also displays these noise sources, which appear as weaker ones (Figures 5a–5e). Finally, the noise model captures changes in the relative importance of microseismic sources at a given time. During both events, the variations in the sharpness of the peak in the beam-former output coincide with changes in the width of the computed source region (compare Figures 4c and 4d with Figures 4e and 4f).

4. Discussion

4.1. Contribution of Ocean Wave Reflection at the Coast to the Noise Generation

[19] The most significant *P* wave sources mapped in Figure 3 occurred in the deep ocean without contribution from ocean wave reflection on the shore. This view is consistent with the previous studies purely based on data analysis [*Gerstoft et al*., 2008]. Note that here we chose to limit our analysis to noise events at teleseismic distance from SCSN (distance larger than 30°), and we therefore do not consider the sources along the coast of North America, such as those documented earlier by *Haubrich and McCamy* [1969]. We performed the computation using a high reflection coefficient $R^2 = 10\%$ at the coast. To make sure that we did not underestimate the effect of the reflection, we also compute all sources for the year 2010 using an unrealistically high reflection coefficient $R^2 = 50\%$ (red line in Figure 2). With the exception of a few new or stronger peaks, increasing the reflection to an unreasonable level does not change much our results and conclusions.

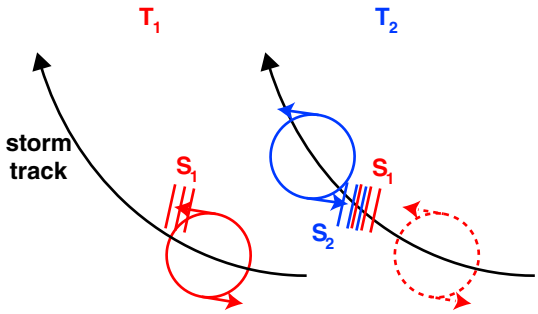

Figure 6. Schematic of the generation of double-frequency microseisms along a storm track. The turning winds in the storm system force a wind sea that then propagates as swell in all directions. Later on, because storms typically travel faster than ocean waves, swell S_1 generated earlier at time T_1 meets swell S_2 generated at T_2, causing wave-wave interactions and noise in the wake of the storm.

4.2. Distribution of Microseismic *P* Wave Sources Versus Sea States

[20] Our numerical model, supported by beam forming analysis, shows that the strongest sources of *P* waves with frequency of 0.193 Hz occur along the usual storm tracks and close to depths of 2800 or 5600 m. More specifically, the source distribution within 90° from the Southern California Seismic Network is dominated by events in the Northern Atlantic and above all in the Northern Pacific. In contrast, we report only four noise bursts in the southern hemisphere (Julian days 73, 76, and 145). The distribution depicted in Figure 3 is in agreement with the previous local [*Koper et al*., 2010] and global studies based on data analysis [*Gerstoft et al*., 2008; *Landes et al*., 2010]. More specifically, our distribution of sources at a frequency of 0.193 Hz in the North Pacific is well correlated with the patch of sources identified by *Koper et al*. [2010] at higher frequency (0.5–2 Hz). The period of significant noise generation in the northern hemisphere as documented here is clearly correlated with local winter (Figure 2) and highest storminess. By analyzing the polarization of microseismic surface waves at stations in the northern hemisphere, *Stutzmann et al*. [2009] also found that northern hemispheric sources dominate during local winter. Following the classification proposed by *Ardhuin et al*. [2011], three situations promote ocean wave interactions responsible for noise generation: within a storm where at rather high frequency, the directional spectra of ocean waves are broad (class I), next to a coast where the incoming ocean waves meet those reflected on the shore (class II), and when a swell meets another swell or a wind sea (class III). The set of events mapped in Figure 3 is too energetic to belong to class I and is not class II either, as discussed above (section 4.1). It mostly represents class III events promoted by frequent storms radiating swells in all directions along nearly the same track.

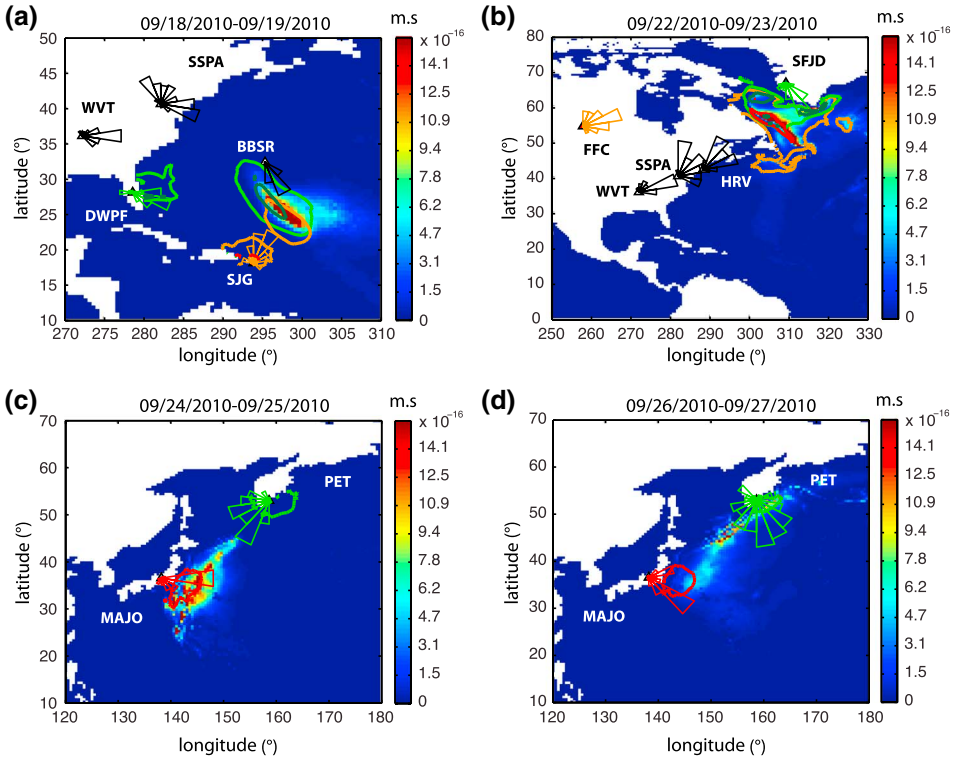

Figure 7. Sources of microseismic surface (Rayleigh) waves during the (a and b) 16 to 23 September 2010 and (c and d) 24 to 27 September 2010 microseismic events. The background images are maps of the surface wave sources (S_{DF} in equation (A1)) generated at 0.193 Hz (the frequency used to compute body waves). The azimuthal histograms show estimates of the incoming direction of the surface waves at GSN (Global Seismic Network) stations close to the storm tracks. These estimates were obtained using a polarization analysis of noise records performed in the range 0.184–0.202 Hz, which covers one frequency step of the wave-noise model around 0.193 Hz. For a selection of stations (those for which the model satisfies the data, see Appendix A), we also show contours of the surface "effective" sources, i.e., taking into account attenuation and geometrical spreading (equation (A2)). Figures 7a and 7b show contours that include 40% (dark red and green lines) and 90% (light red and green lines) of the strongest "effective" sources, while Figures 7c and 7d show contours that include 90% only. Each panel spans a 48 h long period indicated atop of it.

[21] *Zhang et al*. [2010b] detected the signature of strong storms by performing BFA at the SCSN and noticed that the *P* wave source location generally coincides with the wake of the storms, supporting previous results from *Haubrich and McCamy* [1969]. We make the same observation for the two particular events studied here using both BFA and our numerical approach. In the case of the Pacific event, the noise model clearly shows that the storm leaves a "tail" of microseismic sources behind it (see shape of source contours in Figures 4e and 4g). As proposed by *Zhang et al*. [2010b] and illustrated in Figure 6, the gradual motion of the storm, where turning wind excites waves in all directions, creates regions where swell propagate toward the storm and meet waves still being forced in the active wind sea in the opposite direction. The nature of the link between storms and microseisms has implications for noise-based climate studies. While the effect of seismic attenuation blurs the relation between storms and the sources of surface waves effectively recorded at a given station (see discussion in section 4.3), *P* waves appear as rather straightforward indicators of the location of noise-generating storms.

4.3. Comparison Between *P* Wave and Rayleigh Wave Source Distributions

[22] Intrinsically, the distributions of *P* wave and Rayleigh wave sources differ from each other. Appendix A summarizes the theoretical background for microseismic Rayleigh wave generation [*Miche*, 1944; *Longuet-Higgins*, 1950; *Hasselmann*, 1963], and Figure A1 displays the resulting sources for the specific noise event shown in Figure 1d. The distributions shown on these two figures differ owing to a shift toward shallower water of the maximum response in the case of *P* waves, due to the more vertical propagation of sound in the water column compared to Rayleigh modes [*Ardhuin and Herbers*, 2013]. Although the first maximum of the conversion coefficient to *P* wave energy is close to the peak of the coefficient for Rayleigh waves, the second maximum is much narrower and occurs in water depths 10% smaller than the second maximum of Rayleigh waves. For a period of 5 s, this corresponds to depths of 5600 m,

which is close to the depth of the abyssal plains, representing a vast area of the oceans. But for that period, the second Rayleigh-wave peak is at 6200 m depth, which is not very common. This difference may well explain the relative prominence in the deep ocean of *P* waves at 5 s period compared to the Rayleigh waves.

[23] In addition, owing to stronger attenuation for surface than for body waves, the link between sea state-induced microseismic sources and the resulting ground motion at a given station is more complex for surface waves. The two large noise events depicted in Figures 3 and 4 occurred close enough to America and East Asia to produce recordable surface waves at on-shore GSN (Global Seismic Network) stations and illustrate this view (Figure 7). Using the numerical approach of *Ardhuin et al*. [2011], we compute the distribution of the surface wave "effective" sources (equation (A2)), i.e., taking into account severe surface wave attenuation. At a given station, the later may cause weak/close patches of the source region to contribute more than strong/remote patches to the resulting ground displacement (see discussion in Appendix A). To support the numerical results, we perform a polarization analysis [*Schimmel and Gallart*, 2004; *Schimmel et al*., 2011b] at stations in the vicinity of the storm tracks. This analysis highlights a significant level of elliptically polarized noise (i.e., Rayleigh waves) with an incoming direction consistent with the computed source location around the storm system. This is consistent with the results of *Traer et al*. [2012], who found that continental (Earthscope USArray) stations located on the east coast of the U.S. recorded microseismic surface waves incoming from Hurricane Irene, which took place in 2011 along a track similar to our Atlantic storm (Figures 4, 7a, and 7b). In contrast with *P* waves, some of the strongest "effective" sources of surface waves are offset from the storm center. Also, as illustrated by the "effective" source contours in Figure 7, reflection of ocean waves at the coast promotes sources closer to the stations that are thus less attenuated and that contribute more to the recordable noise background than in the case of body waves. For stations SJG and MAJO (Figures 7 and A2), coastal reflection unambiguously generates the strongest "effective" sources.

4.4. Implications for Seismic Imaging Based on Strong Microseismic *P* Sources

[24] Our study demonstrates the ability of numerical noise modeling to provide fast and accurate detection of strong *P* sources, which can subsequently enable travel time estimation, as done by *Zhang et al*. [2010a]. One of the reasons why seismologists have been using noise is to broaden the distribution of seismic sources based initially on earthquakes only. Nevertheless, the sources analyzed here are found to cluster in well-defined areas. It is thus important to note that the broadening of the source distribution is limited if using the strongest noise source only. With that said, this issue can be mitigated by looking at weaker sources, and our numerical approach proves of great interest for that purpose. Using our model as a guide, we were able to report many cases of significant computed sources in the northern Atlantic (for example, 05 February 2010, Table 1) that caused *P* arrivals much less prominent in the beam-former output than simultaneous sources in the Pacific and might have remained unrevealed based solely of data analysis. Because swells propagate over long distances, they are likely to encounter other swells or wind seas away from the usual storm tracks (see, for example, the event described in *Obrebski et al*. [2012]). The sources generated under these specific conditions are expected to be weaker (because interacting swells have been attenuated since they emanated from the storm) and more widely distributed and could be detected by lowering our selection threshold (horizontal line in Figure 2). This observation encourages an extension of the current study, which primary targets are the strongest noise sources.

5. Summary and Conclusions

[25] In this study, we use a numerical model of sea state-induced microseisms to detect and map strong sources of compressional (*P*) body waves. We validate the computed location of sources by performing beam-forming analysis at the Southern California Seismic Network. We provide the first compilation of significant and distributed microseismic *P* sources for this network, which constitute a valuable database to calibrate or test noise-based methods, such as tomography. We describe in more details two particularly strong events that we attribute to storms in the Pacific and Atlantic oceans. Our main conclusions are the following:

[26] 1. The distribution of the strongest sources of *P* waves is highly heterogeneous and is concentrated in well-defined areas.

[27] 2. The strong *P* sources cluster along usual storm tracks in open ocean, mostly without contributions from ocean wave reflection at the coast. Therefore, these noise sources most likely result from the interaction between a swell running into another swell or into a wind sea (class III, as defined in *Ardhuin et al*. [2011]).

[28] 3. We find several examples of microseismic *P* waves emanating directly from storm systems. This simple link between *P* wave sources and storms has practical implications for noise-based climate studies.

[29] 4. The respective distributions of the microseismic sources that make up the body and surface wave wavefields are different, owing to distinctive amplifications of the ocean wave-induced pressure perturbation at the noise source, and different attenuation along seismic paths.

[30] 5. The numerical approach allows targeting microseismic sources in a specific area and time period. Used as a guide, it has thus great potential for beam-forming analysis and noise-based tomography by avoiding random data mining and by simplifying the detection of weaker and more widely distributed sources.

Appendix A: Numerical and Observational Results for Microseismic Surface Waves

[31] Following the theory introduced in section 2.1, for Rayleigh waves, the seismic response for a uniform crust depends on the water depth, crust density, and period:

$$S_{\mathrm{DF}}(f_s) \cong 4\pi^2 f_s \frac{F_{p3D}(f_s)}{\rho_s^2 \beta^5} c_R^2 \tag{A1}$$

where ρ_s is crustal density, β the shear wave speed, and c_R a nondimensional coupling factor (Figure A1a)

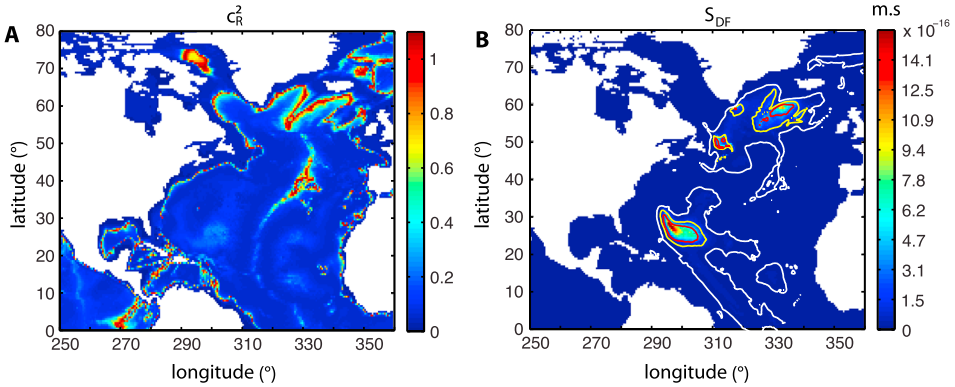

Figure A1. Numerical modeling of wave-induced double-frequency microseismic surface (Rayleigh) waves on 19 September 2010 and at the seismic frequency 0.193 Hz (same event as in Figure 1). (a) Map of the coefficients c_R^2 (equation (A1)) that amplifies the wave-induced pressure into ground displacement associated with Rayleigh waves. (b) Resulting sources (S_{DF} in equation (A1)).

between ocean and crust [*Longuet-Higgins*, 1950]. This response is the rate of increase of the surface vertical ground power spectrum, per unit propagation distance, and will be referred to as the surface wave source for the sake of simplicity.

[32] Here we introduce the distinction between surface wave sources (S_{DF} in equation (A1)) and "effective" sources (see equation (A2)), meaning those that effectively contribute to the resulting ground displacement once taken into account the effect of geometrical spreading and attenuation (quality factor Q) from the source to the receiver. Surface waves are severely affected by attenuation. Therefore, weaker but closer patches of the source region may contribute more than stronger but more remote patches. This does not hold for teleseismic (epicentral distance larger than 30°) body waves for which the attenuation is weaker and the source dimensions are small compared to the source-station distance. Consequently, each individual patch of the source region contributes according to its intensity, almost independently from epicentral distance, and the concept of "effective" sources is not relevant. For Rayleigh waves, the spectrum of the vertical ground displacement observed at longitude λ and latitude φ is obtained by summing the "effective" sources over the area of ocean.

$$F_\delta(\lambda,\varphi,f_s) = \int_{-\pi/2}^{+\pi/2}\int_0^{2\pi} \frac{S_{DF}(f_s)}{R_E \sin\alpha} e^{-2\pi f_s \alpha R_E/(VQ)} R_E^2 \sin\varphi' \, d\lambda' \, d\varphi' \quad \text{(A2)}$$

where V is the seismic group speed, R_E the earth radius, and α the angular distance from the source located at longitude λ' and latitude φ'. Note that a similar expression can be written for the P waves by writing the recorded noise as the sum of the P waves arriving from all oceanic locations [*Ardhuin and Herbers*, 2013, equation (4.45)].

[33] A single value of the quality factor Q is used for computations and is assumed to integrate the effect of the spatially varying attenuation structure of the oceanic and continental crusts. To some extent, Q also absorbs part of the 3-D propagation effects that are not accounted for in our model. Therefore, the values that we adjust for Q must be considered with caution. To obtain synthetic time series (Figure A2), for each event-station pair, we search the values for the reflection coefficient R^2 and Q that minimize the normalized root mean square error between observed and synthetic root mean square vertical ground displacement.

[34] For the two specific events analyzed here, the model satisfies the data (Figure A2) for stations SJG ($Q = 80$, $R^2 = 5.8\%$), DWPF ($Q = 175$, $R^2 = 5.8\%$), FFC ($Q = 400$, $R^2 = 16\%$), MAJO ($Q = 60$, $R^2 = 16\%$), and PET ($Q = 60$, $R^2 = 0$). For the other stations (BBSR, HRV, SSPA, and WVT), all noise peaks correctly appear in the synthetic time series, but we cannot fit their respective amplitude using one single value for Q (from 50 up to 400 for SSPA). We attribute this issue to spatially varying attenuation structure along the storm track and complex 3-D propagation effects (especially around BBSR) that are not accounted for. The model does require coastal reflection for three of six stations (DWPF, MAJO, and SJG). For station FFC, the high R^2 value is an artifact. Overall, the model does not require reflection to fit the data. Nevertheless, a peak appears on day 266 that is not well modeled. Increasing the effect of reflection compensates for this model failure. The distribution of surface wave "effective" sources (equation (A2)) displays a large variety of situations. During the Atlantic event (Figures 7a and 7b), stations SJG and DWPF record surface waves not only from the distant area where the storm and the strongest sources occur but also from closer sources offset from the storm center. At SJG, the reflection at the coast accounts for the local sources, which are the strongest "effective" sources for this station (see 40% contours around SJG in Figure 7a). In the case of DWPF, the local sources presumably result from strong local coupling along a north-south oriented strip off the east coast of North America (Figure A1a). Later on during the Atlantic event, the station SFJD samples sources all over the Labrador Sea but is dominated by the spot located at the south tip of Greenland (40% "effective" source contours in Figure 7b).

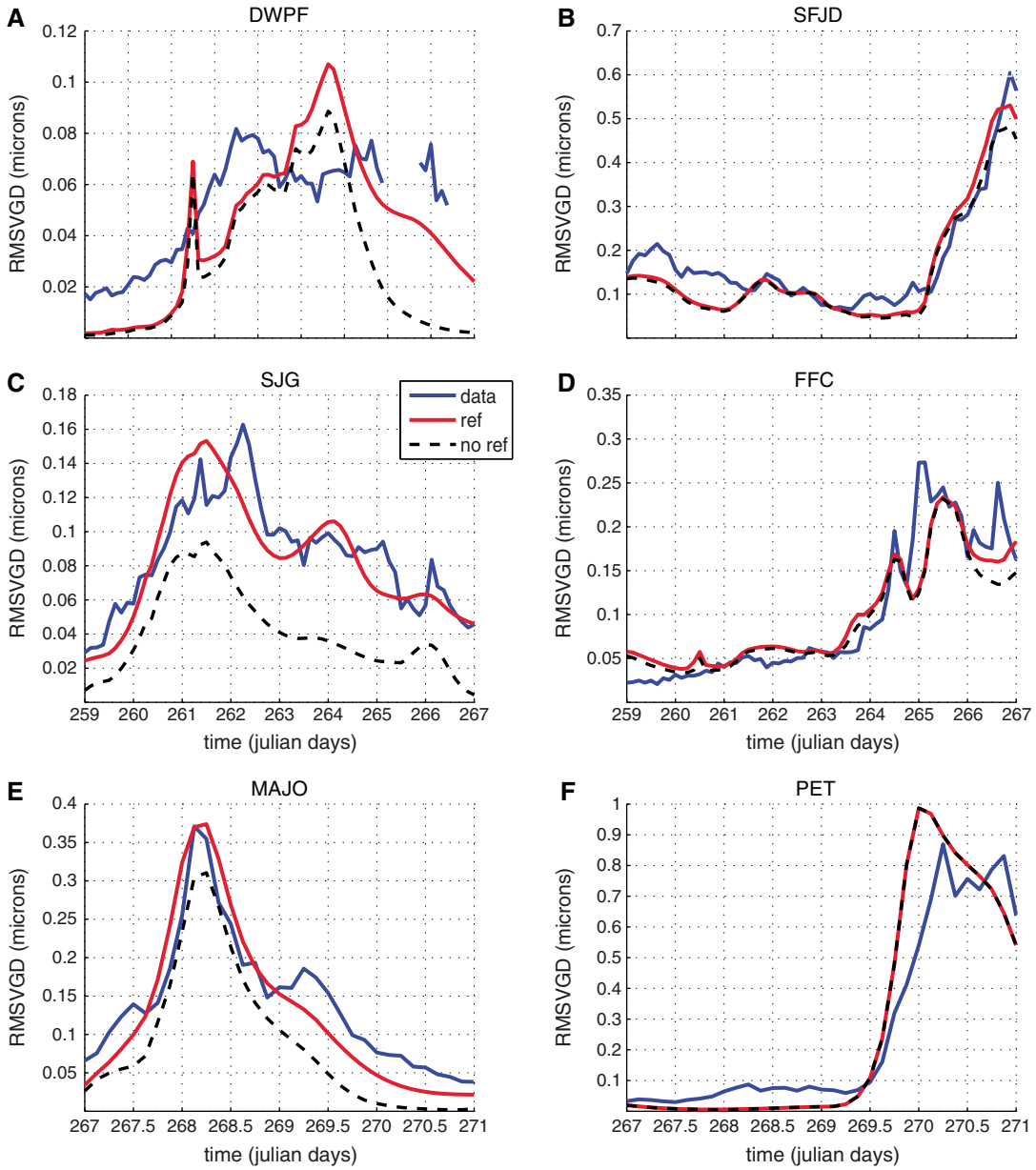

Figure A2. Observed (blue) and computed root mean square vertical ground displacement (RMSVGD) filtered around the frequency 0.193 Hz with (red lines) and without (black dashed lines) taking into account ocean wave coastal reflection during the computation. The computed time series are obtained by summing all "effective" sources of Rayleigh wave (equation (A2)).

[35] **Acknowledgments.** This work was supported by the European Research Council (IOWAGA project), the Program "Investment for the future" Labex Mer (grant ANR-10-LABX-19-01), and the Consolider-Ingeno (Topo-Iberia). M.O. performed the data analysis while visiting the Domaines Océanique laboratory. We thank the editor P. Gerstoft and an anonymous reviewer for their constructive comments. We also thank the operators of Southern California Seismic Network and Global Seismic Network for providing excellent broadband seismic data. Data were obtained from the Southern California Earthquake Data Center.

References

Ardhuin, F., and T. H. C. Herbers (2013), Noise generation in the solid Earth, oceans and atmosphere, from nonlinear interacting surface gravity waves in finite depth, *J. Fluid Mech.*, *716*, 316–348, doi:10.1017/jfm.2012.548.

Ardhuin, F., and A. Roland (2012), Coastal wave reflection, directional spread, and seismoacoustic noise sources, *J. Geophys. Res.*, *117*, C00J20, doi:10.1029/2011JC007832.

Ardhuin, F., et al. (2010), Semi-empirical dissipation source functions for ocean waves. Part I: Definition, calibration, and validation, *J. Phys. Oceanogr.*, *40*, 1917–1941, doi:10.1175/2010JPO4324.1.

Ardhuin, F., E. Stutzmann, M. Schimmel, and A. Mangeney (2011), Ocean wave sources of seismic noise, *J. Geophys. Res.*, *116*, C09004, doi:10.1029/2011JC006952.

Ardhuin, F., A. Balanche, E. Stutzmann, and M. Obrebski (2012), From seismic noise to ocean wave parameters: General methods and validation, *J. Geophys. Res.*, *117*, C05002, doi:10.1029/2011JC007449.

Aster, R., D. McNamara, and P. Bromirski (2008), Multi-decadal climate-induced variability in microseisms, *Seismol. Res. Lett.*, *79*, 194–202, doi:10.1785/gssrl.79.2.194.

Aster, R. C., D. E. McNamara, and P. D. Bromirski (2010), Global trends in extremal microseism intensity, *Geophys. Res. Lett.*, *37*, L14303, doi:10.1029/2010GL043472.

Brenguier, F., M. Campillo, C. Hadziioannou, N. M. Shapiro, R. M. Nadeau, and E. Larose (2008a), Postseismic relaxation along the San Andreas fault at Parkfield from continuous seismological observations, *Science*, *321*(5895), 1478–1481, doi:10.1126/science.1160943.

Brenguier, F., N. Shapiro, M. Campillo, V. Ferrazzini, Z. Duputel, O. Coutant, and A. Nercessian (2008b), Toward forecasting volcanic eruption using seismic noise, *Nat. Geosci.*, *1*, 126–130, doi:10.1038/ngeo104.

Bromirski, P., R. Flick, and N. Graham (1999), Ocean wave height determined from inland seismometer data: Implications for investigating wave climate changes in the NE Pacific, *J. Geophys. Res.*, *104*, 20,753–20,766.

Chevrot, S., M. Sylvander, S. Benahmed, C. Ponsolles, J. M. Lefèvre, and D. Paradis (2007), Source locations of secondary microseisms in western Europe: Evidence for both coastal and pelagic sources, *J. Geophys. Res.*, *112*, B11301, doi:10.1029/2007JB005059.

Durand, S., J. P. Montagner, P. Roux, F. Brenguier, R. M. Nadeau, and Y. Ricard (2011), Passive monitoring of anisotropy change associated with the Parkfield 2004 Earthquake, *Geophys. Res. Lett.*, *38*, L13303, doi:10.1029/2011GL047875.

Ebeling, C. W., and S. Stein (2011), Seismological identification and characterization of a large hurricane, *Bull. Seismol. Soc. Am.*, *101*, 399–403, doi:10.1785/0120100175.

Gerstoft, P., and T. Tanimoto (2007), A year of microseisms in southern California, *Geophys. Res. Lett.*, *34*, L20304, doi:10.1029/2007GL031091.

Gerstoft, P., P. M. Shearer, N. Harmon, and J. Zhang (2008), Global P, PP, and PKP wave microseisms observed from distant storms, *Geophys. Res. Lett.*, *35*, L23306, doi:10.1029/2008GL036111.

Grevemeyer, I., R. Herber, and H.-H. Essen (2000), Microseismological evidence for a changing wave climate in the northeast Atlantic Ocean, *Nature*, *408*, 349–352.

Gualtieri, L., E. Stutzmann, Y. Capdeville, F. Ardhuin, M. Schimmel, A. Mangeney, and A. Morelli (2013), Modelling secondary microseismic noise by normal mode summation, *Geophys. J. Int.*, 1–14, doi:10.1093/gji/ggt090.

Hasselmann, K. (1963), A statistical analysis of the generation of microseisms, *Rev. Geophys.*, *1*, 177–210.

Haubrich, R. A., and K. McCamy (1969), Microseisms: Coastal and pelagic sources, *Rev. Geophys.*, *7*, 539–571.

Haubrich, R. A., W. H. Munk, and F. E. Snodgrass (1963), Comparative spectra of microseisms and swell, *Bull. Seismol. Soc. Am.*, *53*, 27–37.

Hillers, G., N. Graham, M. Campillo, S. Kedar, M. Landès, and N. Shapiro (2012), Global oceanic microseism sources as seen by seismic arrays and predicted by wave action models, *Geochem. Geophys. Geosyst.*, *13*, Q01021, doi:10.1029/2011GC003875.

Kedar, S., M. Longuet-Higgins, F. Webb, N. Graham, R. Clayton, and C. Jones (2008), The origin of deep ocean microseisms in the North Atlantic Ocean, *Proc. R. Soc., Ser. A*, *464*, 777–793, doi:10.1098/rspa.2007.0277.

Kennett, B. L. N., E. R. Engdahl, and R. Buland (1995), Constraints on seismic velocities in the earth from travel times, *Geophys. J. Int.*, *122*, 108–124.

Koper, K. D., and B. de Foy (2008), Seasonal anisotropy in short-period seismic noise recorded in South Asia, *Bull. Seismol. Soc. Am.*, *98*, 3033–3045.

Koper, K. D., B. de Foy, and H. M. Benz (2009), Composition and variation of noise recorded at the Yellowknife Seismic Array, 1991–2007, *J. Geophys. Res.*, *114*, B10310, doi:10.1029/2009JB006307.

Koper, K. D., K. Seats, and H. M. Benz (2010), On the composition of Earth's short period seismic noise field, *Bull. Seismol. Soc. Am.*, *100*, 606–617.

Krim, H., and M. Viberg (1996), Two decades of array signal processing research, *IEEE Signal Process. Mag.*, *13*, 67–94.

Landes, M., F. Hubans, N. Shapiro, A. Paul, and M. Campillo (2010), Origin of deep ocean microseisms by using teleseismic body waves, *J. Geophys. Res.*, *115*, B05302, doi:10.1029/2009JB006918.

Longuet-Higgins, M. (1950), Theory of the origin of microseisms, *Philos. Trans. R. Soc. A*, *243*, 1–35.

Miche, M. (1944), Mouvements ondulatoires de la mer en profondeur constante ou décroissante, *Ann. Ponts Chaussées*, *114*, 131–164.

Obrebski, M. J., F. Ardhuin, E. Stutzmann, and M. Schimmel (2012), How moderate sea states can generate loud seismic noise in the deep ocean, *Geophys. Res. Lett.*, *39*, L11601, doi:10.1029/2012GL051896.

Poli, P., H. A. Pedersen, M. Campillo, and the POLENET/LAPNET Working Group (2012), Emergence of body waves from cross-correlation of short period seismic noise, *Geophys. J. Int.*, *188*, 549–558.

Rivet, D., M. Campillo, N. M. Shapiro, V. Cruz-Atienza, M. Radiguet, N. Cotte, and V. Kostoglodov (2011), Seismic evidence of nonlinear crustal deformation during a large slow slip event in Mexico, *Geophys. Res. Lett.*, *38*, L08308, doi:10.1029/2011GL047151.

Rost, S., and C. Thomas (2002), Array seismology: Methods and applications, *Rev. Geophys.*, *40*(3), 1008, doi:10.1029/2000RG000100.

Roux, P., K. G. Sabra, P. Gerstoft, W. A. Kuperman, and M. C. Fehler (2005), P-waves from crosscorrelation of seismic noise, *Geophys. Res. Lett.*, *32*, L19303, doi:10.1029/2005GL023803.

Sabra, K. G., P. Gerstoft, P. Roux, W. A. Kuperman, and M. C. Fehler (2005), Extracting time-domain Green's function estimates from ambient seismic noise, *Geophys. Res. Lett.*, *32*, L03310, doi:10.1029/2004GL021862.

Schimmel, M., and J. Gallart (2004), Degree of polarization filter for frequency-dependent signal enhancement through noise suppression, *Bull. Seismol. Soc. Am.*, *94*, 1016–1035.

Schimmel, M., E. Stutzmann, and J. Gallart (2011a), Using instantaneous phase coherence for signal extraction from ambient noise data at a local to a global scale, *Geophys. J. Int.*, *184*, 494–506, doi:10.1029/10.1111/j.1365-246X.2010.04861.x.

Schimmel, M., E. Stutzmann, F. Ardhuin, and J. Gallart (2011b), Polarized Earth's ambient microseismic noise, *Geochem. Geophys. Geosyst.*, *12*, Q07014, doi:10.1029/2011GC003661.

Shapiro, N. M., and M. Campillo (2004), Emergence of broadband Rayleigh waves from correlations of the ambient seismic noise, *Geophys. Res. Lett.*, *31*, L07614, doi:10.1029/2004GL019491.

Shapiro, N., M. Campillo, L. Stehly, and M. H. Ritzwoller (2005), High-resolution surface-wave tomography from ambient seismic noise, *Science*, *307*, 1615–1618.

Stutzmann, E., M. Schimmel, G. Patau, and A. Maggi (2009), Global climate imprint on seismic noise, *Geochem. Geophys. Geosyst.*, *10*, Q11004, doi:10.1029/2009GC002619.

Stutzmann, E., F. Ardhuin, M. Schimmel, A. Mangeney, and G. Patau (2012), Modelling long-term seismic noise in various environments, *Geoph. J. Int*, doi:10.1111/j.1365-246X.2012.05638.x.

Tolman, H. L. (2008), A mosaic approach to wind wave modeling, *Ocean Modell.*, *25*, 35–47.

Traer, J., P. Gerstoft, P. D. Bromirski, and P. M. Shearer (2012), Microseisms and hum from ocean surface gravity waves, *J. Geophys. Res.*, *117*, B11307, doi:10.1029/2012JB009550.

Zhang, J., P. Gerstoft, and P. Shearer (2010a), Resolving P-wave travel-time anomalies using seismic array observations of oceanic storms, *Earth Planet. Sci. Lett.*, *292*, 419–427.

Zhang, J., P. Gerstoft, and P. D. Bromirski (2010b), Pelagic and coastal sources of P-wave microseisms: Generation under tropical cyclones, *Geophys. Res. Lett.*, *37*, L15301, doi:10.1029/2010GL044288.